Re-analysis of temperature dependent neutron capture rates and stellar β-decay rates of $^{95\text{-}98}$Mo

Abdul Kabir[1†] Jameel-Un Nabi[2] Muhammad Tahir[2] Abdul Muneem[3] Zain Ul Abideen[1]

[1]Space and Astrophysics Research lab, National Centre of GIS and Space Applications, Department of Space Science, Institute of Space Technology, Islamabad 44000, Pakistan
[2]University of Wah, Quaid Avenue, Wah Cantt 47040, Punjab, Pakistan
[3]Faculty of Engineering Sciences, GIK Institute of Engineering Sciences and Technology, Topi 23640, Khyber Pakhtunkhwa, Pakistan

Abstract: The neutron capture rates and temperature dependent stellar beta decay rates of Mo isotopes are investigated within the framework of the statistical code TALYS v1.96 and the proton neutron quasi particle random phase approximation (*pn*-QRPA) model. The Maxwellian average cross-section (MACS) and neutron capture rates for the $^{95-98}$Mo$(n,\gamma)^{96-99}$Mo radiative capture process are analyzed within the framework of the statistical code TALYS v1.96 based on the phenomenological nuclear level density model and gamma strength functions. The present model-based computations for the MACS are comparable to the existing measured data. The sensitivity of stellar weak interaction rates to various densities and temperatures is investigated within the framework of the *pn*-QRPA model. Particular attention is paid to the impact of thermally filled excited states in the decaying nuclei ($^{95-98}$Mo) on electron emission and positron capture rates. Furthermore, we compare the neutron capture rates and stellar beta decay rates. It is found that neutron capture rates are higher than stellar beta decay rates at both lower and higher temperatures.

Keywords: cross-section, TALYS, nuclear level density, decay rates, capture rates

DOI: 10.1088/1674-1137/ad5428

I. INTRODUCTION

The energy production in stars [1] and the associated nucleosynthesis [2–4] as well as supernova explosion dynamics [5] are still not fully understood. Nuclei heavier than iron are mostly formed by neutron capture processes, either the slow neutron capture process (*s*-process) or rapid neutron capture process (*r*-process) [2, 3]. Here, the terms slow and rapid consider whether neutron capture proceeds at rates lower or higher than those of typical beta decays occurring along the respective nucleosynthesis path. Slow neutron capture (in particular, that including isotopes across and beyond the neutron magic number $N = 50$ up to $N = 126$) is attributed to the final evolutionary stages of red giants (called asymptotic giant branch (AGB) stars). The *s*-process takes place when $0.3 < T_9 < 1$ and the neutron density $N_n \approx 10^8$ cm^{-3} [6].

In this paper, we focus on the competition between the $^{95-98}$Mo$(n,\gamma)^{96-99}$Mo and $^{95-98}$Mo$\rightarrow$ $^{95-98}$Tc $+ e + \nu_e$ processes within the framework of the statistical code TALYS v1.96 and the proton neutron quasi particle random phase approximation (*pn*-QRPA) model. The Maxwellian averaged cross-section (MACS) of $^{95-98}$Mo is a crucial quantity in determining the radiative neutron capture rates. Many researchers have theoretically and experimentally studied the neutron capture cross-sections of Mo isotopes at different energy ranges [7–10]. Saumi *et al.* [7] studied the MACS for the nuclei participating in the *s*-process and *p*-process nucleosynthesis around $N = 50$. They constructed a microscopic optical-model potential by the folding DDM3Y nucleon-nucleon interaction with the radial matter density of the target obtained from the relativistic mean-field (RMF) approximation. Their computed MACSs at $kT = 30$ keV for $^{95-98}$Mo$(n,\gamma)^{96-99}$Mo were 212, 113, 299, and 73.8 mb, respectively. The neutron capture cross-sections of seven stable isotopes of Mo have been measured using a 40 m station of the Oak Ridge Electron Linear Accelerator (ORELA) in the energy range ($3 < E_n < 90$) keV [11]. Recently [12], the capture cross-section and transmission of natural Mo were studied using an accurate neutron-nucleus reaction measurement instrument (ANNRI) situated in the Material Life and Science Facility (MLF) at J-PARC. Experimental analyses of capture cross-sections for ^{94,95,96}Mo isotopes have been conducted at the neutron time-of-flight facilities n_TOF at CERN and GELINA at JRC-Geel using samples with an enrichment

Received 12 February 2024; Accepted 5 June 2024; Published online 6 June 2024
† E-mail: kabirkhanak1@gmail.com

exceeding 95% for each isotope [13]. The transmission parameters obtained in the experiment have been used to validate the resonance parameter files for Mo isotopes. Massimi *et al*. [14] measured the neutron capture cross-section in EAR1 and EAR2 at the n_TOF facility to reduce the uncertainty in the presently known data for the stable ^{94,95,96}Mo isotopes. ^{98}Mo is the stable and most abundant isotope, with an abundance of 24.13%. Understanding the thermal neutron cross-section and resonance integral for the ^{98}Mo$(n,\gamma)^{99}$Mo reaction is crucial owing to the utilization of neutron activation cross-section data in the production of ^{99}Mo and its potential applications in various studies related to neutron-matter interactions [15]. The existing literature contains numerous experimental and evaluated datasets on the thermal neutron capture cross-section and resonance integrals for the ^{98}Mo$(n,\gamma)^{99}$Mo reaction. The authors in Ref. [16] studied the cross-section of ^{98}Mo$(n,\gamma)^{99}$Mo using a monochromatic thermal neutron beam at low energy. Their obtained cross-sections were 116±7 and 91±5 mb at energies of 0.0334 and 0.0536 eV, respectively.

The nuclei ($^{95-98}$Mo) suggested in the present work are stable isotopes of Mo at the terrestrial environment. The temperature conditions that exist in the stellar matter are so intense (10^9 K) that the excited states of parent nuclei have considerable occupation probability. Thus, the individual excited states make measurable contributions to the total stellar weak rates [17]. Therefore, the method based on microscopic calculation of rates must include the contributions of all the partial decay rates due to individual parent excited states. This state by state evaluation of weak-interaction mediated rates is the foundation of the *pn*-QRPA model [18]. The first attempts to calculate the microscopic weak interaction rates for a large number of available nuclei far away from the stability line were performed using the *pn*-QRPA approach. The *pn*-QRPA approach can be formulated based on the mean-field basis employing varying forms of potential. Noticeable mentions would include the deformed Nilsson model [19–21], the finite-range droplet model with a folded Yukawa single-particle potential [22, 23], and the Woods–Saxon potential [24, 25].

The present study is structured as follows: Sec. II provides a quick overview of the basic formalism for the statistical code (TALYS v1.96) and the *pn*-QRPA model. Sec. III summarizes the results of our calculations and how they compare to previous findings and measurements. Our findings are summarized in Sec. IV.

II. THEORETICAL FRAMEWORK

A. TALYS v1.96 code

The TALYS v1.96 code [26] is based on the Hauser-Feshbach theory [27, 28]. The main inputs in the Hauser-Feshbach theory are the nuclear level densities (NLDs), optical model potentials (OMPs), and gamma strength functions (GSFs). The effect of altering the OMPs can be disregarded in favor of the other two components when low-energy neutrons are used as incident particles [29]. The optical model employed in this study is the local OMP [30].

The TALYS v1.96 code used for the simulation of nuclear reactions includes several state of the art nuclear models to cover almost all key reaction mechanisms encountered for light particle-induced nuclear reactions. It provides an extensive range of reaction channels. The possible incident particles can be simulated in the E_i = (0.001−200) MeV, and the target nuclides can be from A = 12 onwards. The output of the nuclear reaction includes total cross-sections, angular distributions, energy spectra, double-differential spectra, MACSs, and capture rates. Radiative capture is important in the context of nuclear astrophysics in which a projectile fuses with the target nucleus and emits γ-ray [31–35]. The MACS is used when the energies of the projectiles follow a Maxwellian distribution, such as that in a stellar enviroment. The MACS is an average of the cross-section over a range of energies, weighted by the Maxwell-Boltzmann distribution.

$$\langle\sigma\rangle(kT) = \frac{2}{\sqrt{\pi}(kT)^2}\int_0^{\infty} E\sigma(E)\exp\left(\frac{-E}{kT}\right)\mathrm{d}E, \qquad (1)$$

where k is the Boltzmann constant, T is the temperature, $\sigma(E)$ is the capture cross-section, and E is the projectile energy. In statistical models for predicting nuclear reactions, level densities are needed at excitation energies where experimental information is not available, and they have to be taken from theoretical model predictions. Together with the OMP, a correct level density is perhaps the most crucial ingredient for a reliable theoretical analysis of cross-sections, angular distributions, and other nuclear quantities. NLDs are crucial structure ingredients in statistical computations. In the cases where experimental information is not available, they have to be taken from theoretical model predictions. In the present analysis, we employed the back-shifted Fermi gas model (BSFM) as the NLD. The BSFM was used for the entire energy range by treating the pairing energy as an adjustable parameter

$$\rho_F^{\mathrm{tot}}(E_x) = \frac{1}{\sqrt{2\pi}\sigma}\frac{\sqrt{\pi}}{12}\frac{\exp(2\sqrt{aU})}{a^{1/4}U^{5/4}}, \qquad (2)$$

where σ is the spin cut-off parameter, which represents the width of the angular momentum distribution, U is the effective excitation energy, and a is the level density parameter defined below:

$$a = \tilde{a}\left(1+\delta W\frac{1-\exp(-\gamma U)}{U}\right), \quad \text{where } \tilde{a} = \alpha A + \beta A^{2/3}, \tag{3}$$

where $\tilde{a}$ is the asymptotic level density without any shell effects, A is the mass number, and α, β, and γ are global parameters that need to be determined to give the best average level density description over a whole range of nuclides. δW gives the shell correction energy, and the damping parameter γ determines how rapidly a approaches to $\tilde{a}$. For the best fitting, one can readjust the a to achieve the desired value of cross-section and nuclear reaction rates. For further investigations, one can refer to [36]. Different GSFs are included in TALYS v1.96; among them, the Brink-Axel model is used for all transitions except for $E1$ [26]. The GSF f_{XL} for the Brink-Axel gives the distribution of the average reduced partial transition width as a function of the photon energy E_γ

$$f_{XL}(E_\gamma) = K_{XL}\frac{\sigma_{XL}E_\gamma\Gamma_{XL}^2}{(E_\gamma^2-E_{XL}^2)^2+(E_\gamma\Gamma_{XL}^2)^2}, \tag{4}$$

where E_{XL} is the energy, Γ_{XL} is the width, and σ_{XL} is the giant resonance strength. For $E1$ transitions, TALYS v1.96 utilizes the Kopecky-Uhl model by default

$$f_{XL}(E_\gamma,T) = K_{XL}\left[\frac{E_\gamma\tilde{\Gamma}_{E1}(E_\gamma,T)}{(E_\gamma^2-E_{E1}^2)^2+E_\gamma^2\tilde{\Gamma}_{E1,T}(E_\gamma)^2} + \frac{0.7\Gamma_{E1}4\pi^2T^2}{E_{E1}^3}\right]\sigma_{E1}\Gamma_{E1}, \tag{5}$$

and

$$\tilde{\Gamma}_{E1}(E_\gamma,T) = \Gamma_{E1}\frac{E_\gamma^2+4\pi^2\dfrac{E_n+S_n-\Delta-E_\gamma}{a(S_n)}}{E_{E1}^2}, \tag{6}$$

where $\tilde{\Gamma}(E_\gamma)$ represents the energy-dependent damping width, E_n is the incident energy of neutrons, S_n is the neutron seperation energy, and Δ is the correction for pairing. As mentioned earlier, a represents the level density parameter at S_n. The Gogny-HFB+QRPA dipole strength function is employed for the large-scale calculations of the $E1$ and $M1$ absorption γ-ray strength function within the framework of the axially symmetric deformed quasiparticle random phase approximation (QRPA) based on the finite range D1M Gogny force to the de-excitation strength function [37]. The final $E1$ and $M1$ strengths, including low-energy contributions (D1M+QRPA+0lim), can be stated as follows:

$$f_{E1}(\varepsilon_\gamma) = f_{E1}^{\rm QRPA}(\varepsilon_\gamma) + f_0U/[1+e^{(\varepsilon_\gamma-\varepsilon_0)}] \tag{7}$$

$$f_{M1}(\varepsilon_\gamma) = f_{M1}^{\rm QRPA}(\varepsilon_\gamma) + Ce^{-\eta\varepsilon_\gamma}, \tag{8}$$

where $f_{X1}^{\rm QRPA}$ is the D1M+QRPA dipole strength at the photon energy ε_γ, and U is the excitation energy of the initial de-exciting state. f_0, ε_0, C, and η are freely adjustable parameters.

B. *pn*-QRPA model

The stellar beta decay rates are investigated within the framework of the *pn*-QRPA. The Hamiltonian for the model is expressed as

$$H^{\rm QRPA} = H^{sp} + V^{\rm pair} + V_{\rm GT}^{ph} + V_{\rm GT}^{pp}. \tag{9}$$

The deformed Nilsson potential (H^{sp}) basis is utilized to compute the wave functions and single particle energies. Pairing forces are represented by the second term of Eq. (9) within the framework of the Bardeen–Cooper–Schrieffer (BCS) approximation. Q-values and residual interactions have a considerable influence on the computed electron emission (β^-) rates and associated half-lives [38]. $V_{\rm GT}^{ph}$ (χ (ph)) and $V_{\rm GT}^{pp}$ (κ (pp)), known as the residual interactions, are taken into account for the calculation of the Gamow Tellar (GT) strength. For a thorough definition of χ and κ, as well as the optimal choice of these parameters, see Refs. [38–40].

The $V_{\rm GT}^{ph}$ interaction is expressed as

$$V_{\rm GT}^{ph} = +2\chi\sum_{\mu=-1}^{1}(-1)^\mu Y_\mu Y_{-\mu}^\dagger, \tag{10}$$

with

$$Y_\mu = \sum_{j_pm_pj_nm_n} < j_pm_p \mid t_-\,\sigma_\mu \mid j_nm_n > c_{j_pm_p}^\dagger c_{j_nm_n}, \tag{11}$$

whereas the $V_{\rm GT}^{pp}$ interaction is defined as

$$V_{\rm GT}^{pp} = -2\kappa\sum_{\mu=-1}^{1}(-1)^\mu P_\mu^\dagger P_{-\mu}, \tag{12}$$

with

$$P_\mu^\dagger = \sum_{j_pm_pj_nm_n} < j_nm_n \mid (t_-\sigma_\mu)^\dagger \mid j_pm_p > \times(-1)^{l_n+j_n-m_n}c_{j_pm_p}^\dagger c_{j_n-m_n}^\dagger, \tag{13}$$

where χ and κ are taken from Ref. [40]. Reduced GT

transition probabilities are achieved by expressing the QRPA ground state into one-phonon states in the daughter nucleus. Additional input variables for the calculation of weak transitions include the pairing gap (Δ_p, Δ_n), nuclear deformation (β_2), threshold-values of energy, and Nilsson potential variables (NPV). We adjusted our computation with nuclear deformation parameters from the most recent analysis [41]. The NPV is taken from [42], and the oscillation constant (which is similar for protons and neutrons) is determined using the equation $\hbar\omega = 41A^{-1/3}$ (in MeV). We employed the Nilsson potential for the analysis of the wave functions. β_2 is used as an input parameter in the Nilsson potential. Primarily, wave functions and single particle energies are calculated on the deformed Nilsson basis. The transformation from the spherical nucleon basis (c^{+}_{jm}, c_{jm}) to the axial symmetric deformed basis ($d^{+}_{m\alpha}$, $d_{m\alpha}$) is performed as follows:

$$d^{+}_{m\alpha} = \sum_{j} D^{m\alpha}_{j} c^{+}_{jm}, \tag{14}$$

where $D^{m\alpha}_{j}$ is a group of Nilsson eigenfunctions with α as an additional quantum number to characterize the Nilsson eigen-states. The BCS formalism is used in the Nilsson basis for the neutron/proton system separately. The diagonalization of the Nilsson Hamiltonian yields the transformation matrices (a detailed explanation can be found in [39, 43]). The globally systematic pairing gap values, Δ_n=Δ_p=$12/\sqrt{A}$ (MeV), are employed in our computation. The Q-values are obtained from the most current assessment of atomic mass data [44]. Further details of Eq. (9) may be obtained from [45]. The computation of terrestrial beta decay half-lives and further information on the formalism utilized to estimate GT transitions in stellar scenarios using the *pn*-QRPA technique can be found in Refs. [46, 47].

The electron emission rates/positron capture rates ($\lambda^{(\beta^{-}/pc)}_{ij}$) from the parent nucleus (ith-state) to the daughter nucleus (jth-state) is given by

$$\lambda^{(\beta^{-}/pc)}_{ij} = \ln 2 \frac{f_{ij}(T,\rho,E_f)}{(ft)_{ij}}, \tag{15}$$

where $(ft)_{ij}$ is related to the reduced transition probability (B_{ij}) by

$$(ft)_{ij} = D/B_{ij}, \tag{16}$$

D is taken as 6143 s [48], and B_{ij} is defined as

$$B_{ij} = B(F)_{ij} + (g_A/g_V)^2 B(GT)_{ij}, \tag{17}$$

where $B(F)$ and $B(GT)$ are the Fermi and Gamow Teller reduced transition probabilities, respectively. f_{ij} is the phase space factor. Further details can be found in Ref. [47]. Due to the high temperature in the stellar core, β^{-} and positron capture (pc) rates receive only a minor contribution from parent excited energy levels. We utilize the Boltzmann distribution function to compute the occupancy probability of the parent ith-state:

$$P_i = \frac{\exp(-E_i/kT)}{\sum_{i=1}\exp(-E_i/kT)}. \tag{18}$$

Furthermore, the total stellar β^{-}/pc rates are computed using

$$\lambda^{(\beta^{-}/pc)} = \sum_{ij} P_i \lambda^{(\beta^{-}/pc)}_{ij}. \tag{19}$$

The summation stands for the computation of all parent and daughter energy levels until the required and desired convergence is achieved. In our present calculations, the large model space (up to 7 $\hbar\omega$ major oscillatory shells) makes it easier to achieve the desired convergence. The ability to calculate the weak rates of any heavy nuclear species is one of the main advantages of the *pn*-QRPA technique.

C. Stellar neutron capture rates ($\lambda_{(n,\gamma)}$)

The total neutron capture rate ($\lambda_{(n,\gamma)}$ in the units of s^{-1}) is defined as [49]

$$\lambda_{(n,\gamma)} = (v_i \times \sigma_i \times n_n)\, s^{-1}, \tag{20}$$

where v_i is the averaged neutron velocity, σ_i is the MACS, and n_n is the average neutron density for $T_9 < 1$.

$$n_n = \frac{4.3\times10^{36}\rho X_4 e^{[-(0.197/T_9)^{4.82}]}(\frac{1}{T_9})^{2/3} e^{\frac{-47}{(T_9)^{1/3}}}}{\sigma_{22}[1+\sigma_i N_i/\Sigma\sigma_{22}N_{22}](\frac{T_9}{0.348})^{1/2}}\ \mathrm{cm}^{-3}, \tag{21}$$

where X_4 is the helium mass fraction, ρ is the nuclear matter density, and T_9 is the temperature at the base of the convective shell. σ_{22} is the ^{22}Ne$(n,\gamma)^{23}$Ne capture cross-section. N_i is the abundance of species i, and σ_i is the MACS. N_{22} is the abundance by mass of ^{22}Ne. We have chosen $\rho = 10^4$ g cm^{-3}, $X_4 = 0.2$, and σ_{22}= 0.4 mb for the calculations of average neutron density. The composition of heavy nuclei at the base of the convective shell is dominated by ^{22}Ne produced by α- captures on ^{14}N from the CNO cycle.

III. RESULTS AND DISCUSSION

For some applications, such as astrophysical investigations involving nuclei along neutron or proton drip

lines, it is crucial to extrapolate the data much beyond the experimentally known region. The NLD and GSFs can now be tested on the experimental data relative to the radiative neutron-capture cross-sections of the $^{95-98}$Mo$(n,\gamma)^{96-99}$Mo process. These cross-sections essentially depend on the photon transmission coefficient of the final compound nucleus. Because experiments cannot be conducted at all energies, it is evident that theoretical extrapolations are important for the radiative capture processes. In the present analysis, we employed the NLD model (BSFM) and GSFs (Brink-Axel, Gogny, and Kopecky-Uhl) for the computation of the MACSs of $^{95-98}$Mo. The present-listed Mo isotopes are beta stable in terrestrial environments. Moreover, they have almost stable neutron number configurations, which result in their small (n,γ) cross-sections. For the calculation of MACSs for $^{95-98}$Mo$(n,\gamma)^{96-99}$Mo, we fixed the BSFM for the NLD and Brink-Axel, Gogny, and Kopecky-Uhl for the GSFs. Together with the findings of Ref. [50], the MACSs for ^{95,97}Mo$(n,\gamma)^{96,98}$Mo within $(0.01 < kT < 100)$ keV are depicted in Fig. 1(A), (B). The computed results based on the present model agree well with the data in Ref. [50], and both are below or above the *s*-process energy (kT= 30 keV). Note that, in order to achieve the best-fitting with the measured data, we adjusted the parameter a as mentioned in Eq. (3). In the present case, the adjustment parameter a is determined to be 0.5 through adjustment to all available experimental data of the MACS. Similarly, the ^{96,98}Mo$(n,\gamma)^{97,99}$Mo radiative capture processes are analyzed using the BSFM for the NLD and Brink-Axel, Gogny, and Kopecky-Uhl for the GSF. The energy dependent MACSs for ^{96}Mo and ^{98}Mo isotopes are depicted in Fig. 2(A), (B) along with the results of Ref. [50]. The computed MACSs at kT = 30 keV for the analysis of ^{96}Mo$(n,\gamma)^{97}$Mo are 121.35 mb (Brink-Axel for the GSF), 124.31 mb (Gogny for the GSF), and 152.29 mb (Kopecky-Uhl for the GSF). It is observed that the present model-based results agree well with the 113 mb MACS at kT = 30 keV from Ref. [50]. Similarly, the computed MACSs at kT = 30 keV for the analysis of ^{98}Mo$(n,\gamma)^{99}$Mo are 101.28 mb (Brink-Axel for the GSF), 98.42 mb (Gogny for the GSF), and 78.80 mb (Kopecky-Uhl for the GSF). Remarkably, at kT = 30 keV, the current model-based results agree well with the MACS reported in Ref. [50].

As mentioned earlier, the nuclei ($^{95-98}$Mo) in the present work are stable isotopes of Mo at the terrestrial enviroment. However, the temperature conditions that exist in the stellar enviroment are so intense that the excited states of parent nuclei are highly likely to be occupied. Each excited state contributes measurably to the cumulative stellar weak rates. As a result, the approach based on microscopic rate computation must incorporate the contributions of all partial decay rates attributable to the individual parent excited state. For this purpose, we employed the the *pn*-QRPA framework. The *pn*-QRPA Hamiltonian defined by Eq. (9) has Nilsson deformed potential and residual interaction terms. In the present study, we employed the nuclear deformation (β_2) from the finite range droplet model (FRDM) [41] as an input parameter for our *pn*-QRPA model based calculations. The β_2

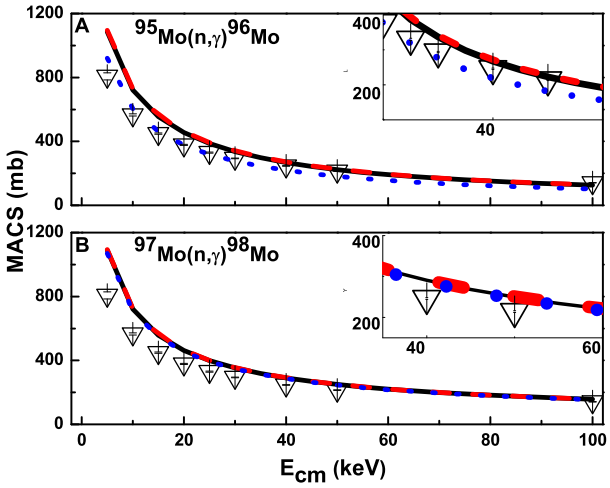

Fig. 1. (color online) Total MACS for ^{95,97}Mo(n,γ) ^{96,98}Mo along with the measured data (▽) [50]. (A) MACS for ^{95}Mo$(n,\gamma)^{96}$Mo computed by the BSFM for the NLD with Brink-Axel (solid line), Gogny (dashed line), and Kopecky-Uhl (dotted line) for the GSFs. (B) MACS for ^{97}Mo$(n,\gamma)^{98}$Mo computed by the BSFM for the NLD with Brink-Axel (solid line), Gogny (dashed line), and Kopecky-Uhl (dotted line) for the GSFs.

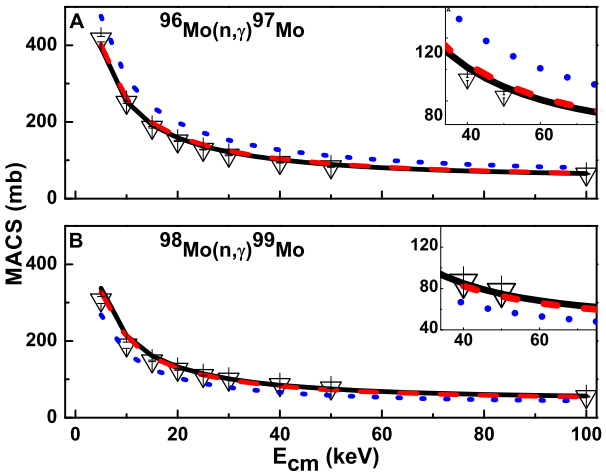

Fig. 2. (color online) Total MACS for ^{96,98}Mo(n,γ) ^{97,99}Mo along with the measured data (▽) [50]. (A) MACS for ^{96}Mo$(n,\gamma)^{97}$Mo computed by the BSFM for the NLD with Brink-Axel (solid line), Gogny (dashed line), and Kopecky-Uhl (dotted line) for the GSFs. (B) MACS for ^{98}Mo$(n,\gamma)^{99}$Mo computed by the BSFM for the NLD with Brink-Axel (solid line), Gogny (dashed line), and Kopecky-Uhl (dotted line) for the GSFs.

values are 0.000 (^{95}Mo), 0.150 (^{96}Mo), 0.172 (^{97}Mo), and 0.206 (^{98}Mo). The residual interaction χ and κ values in the present cases are optimized based on Ref. [40] and completely satisfy the model-independent Ikeda sum rules. Based on the optimized values of the residual interactions, we computed the electron emission and positron capture rates. The results of our present investigations are presented in Figs. 3–6 (A)–(C) at densities $\rho = (10^3$–$10^5)$ g cm^{-3}. It is obvious from the results that the electron emission rates are higher than the positron capture rates at lower and higher temperatures. At low density, $\rho = 10^3$ g cm^{-3}, and low temperatures, the λ_{β^-} values are higher than the λ_{pc} values; however, at high temperatures, λ_{pc} increases gradually because the positron is created at high temperatures. For ^{95}Mo, there is a clear difference between the λ_{pc} and λ_{β^-} values at higher densities, as mentioned in Figs. 3–6 (A)–(C). Similarly, Figs. 4–6 (A)–(C) depict the λ_{pc} and λ_{β^-} values for $^{96-98}$Mo at $\rho = (10^3$–$10^5)$ g cm^{-3}. We noted that the stellar beta decay rates increase with temperature, but for the cases of heavier nuclei of Mo, λ_{pc} and λ_{β^-} are almost the same at higher temperatures.

Furthermore, we computed the temperature-dependent neutron capture rates ($\lambda_{(n,\gamma)}$) for $^{95-98}$Mo. For the calculations of $\lambda_{(n,\gamma)}$, we employed Eq. (20). In the initial set of computations, we identified the best-fitting model combination (in TALYS v1.96) for each isotope; in our investigation, this combination is Brink-Axel as the GSF and BSFM as the NLD. Based on the relevant MACSs, we computed $\lambda_{(n,\gamma)}$. At $kT = 30$ keV, the present computed MACSs for ^{95}Mo and ^{97}Mo are 276 and 347 mb, respectively. Employing these cross-sections, the total neutron capture rates for ^{95}Mo and ^{97}Mo are $\lambda_{(n,\gamma)} = (6.60\times10^{-17}\ n_n)$ s^{-1} and $\lambda_{(n,\gamma)} = (8.305\times10^{-17}\ n_n)$ s^{-1}, respectively. Similarly, at $kT = 30$ keV, the MACSs for ^{96}Mo and ^{98}Mo are 121 and 98 mb, respectively. With these cross-sections, the total capture rates for ^{96}Mo and ^{98}Mo are $\lambda_{(n,\gamma)} = (2.90\times10^{-17}\ n_n)$ s^{-1} and $\lambda_{(n,\gamma)} = (2.34\times10^{-17}\ n_n)$ s^{-1}, respectively. At $\rho = 10^4$ g cm^{-3} and $X_4 = 0.2$, the present computed $\lambda_{(n,\gamma)}$ and $\lambda_{(\beta^-+pc)}$ values are depicted in Fig. 7 (A)–(D) for the $^{95-98}$Mo + n → $^{96-99}$Mo + γ and $^{95-98}$Mo → $^{95-98}$Tc + e + ν_e. Evidently, at lower temperatures, the thermally enhanced beta decay rates are much lower in magnitude than $\lambda_{(n,\gamma)}$. For example, at $T_9 = 0.1$, $\lambda_{(n,\gamma)} = 5.1\times10^{-31}$ s^{-1}, whereas at the same temperature, $\lambda_{(\beta^-+pc)}$ is 0.97×10^{-100} s^{-1} for ^{95}Mo. Similarly, at $T_9 = 0.5$, $\lambda_{(n,\gamma)} = 3.5\times10^{-02}$ s^{-1} and $\lambda_{(\beta^-+pc)}$ is 2.37×10^{-26} s^{-1}. For ^{97}Mo, at $T_9 = 0.1$, $\lambda_{(n,\gamma)} = 6.4\times10^{-31}$ s^{-1}, whereas at the same temperature, $\lambda_{(\beta^-+pc)}$ is 5.5×10^{-56} s^{-1}. However, at $T_9 = 0.5$, $\lambda_{(n,\gamma)} = 4.4\times10^{-02}$ s^{-1} and $\lambda_{(\beta^-+pc)}$ is 1.37×10^{-15} s^{-1}. In the examined situations of

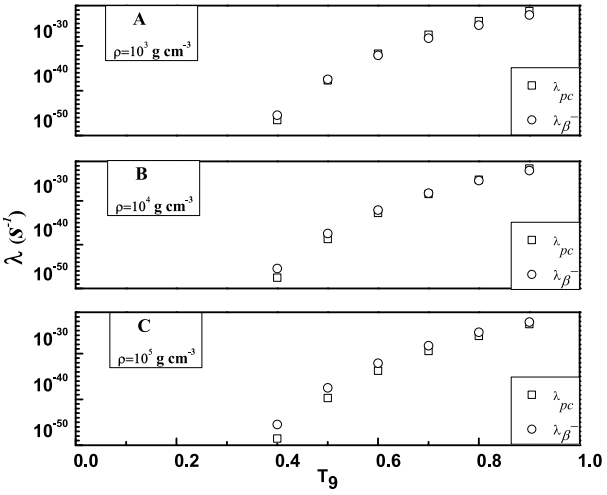

Fig. 4. λ_{pc} and λ_{β^-} at all densities for the beta decay of ^{96}Mo.

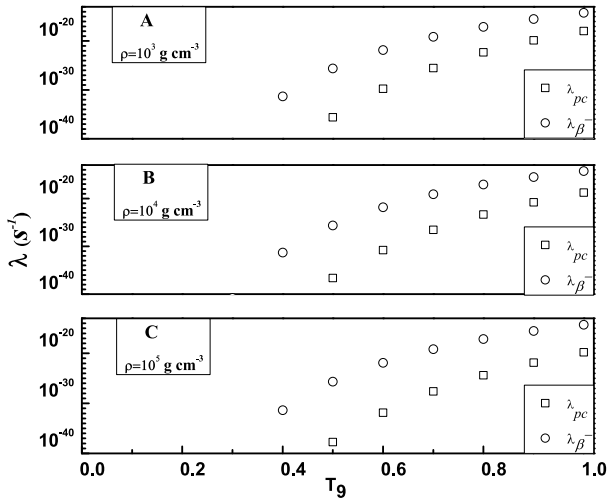

Fig. 3. λ_{pc} and λ_{β^-} at all densities for the beta decay of ^{95}Mo.

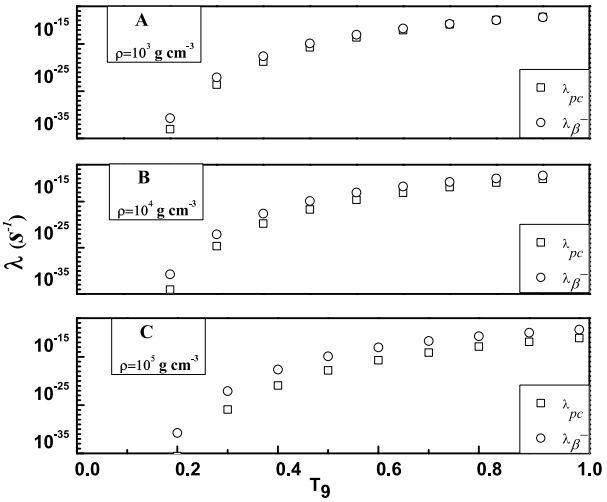

Fig. 5. λ_{pc} and λ_{β^-} at all densities for the beta decay of ^{97}Mo.

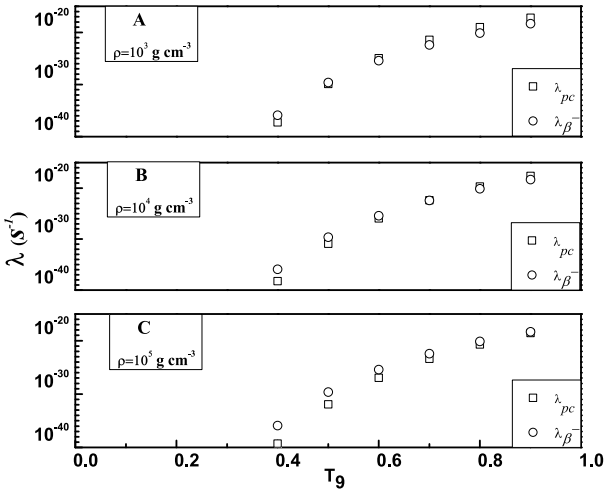

Fig. 6. λ_{pc} and λ_{β} at all densities for the beta decay of ^{98}Mo.

Mo nuclei, the neutron capture rates exceed the thermally enhanced beta decay rates both at lower and higher temperatures.

IV. CONCLUSION

The main findings and inferences are summarized as follows.

1. We examined the MACSs of the (n,γ) process for sets of stable Mo nuclei with magic or nearly magic neutron numbers in the context of the TALYS v1.96 code across a broad energy range. We deduced that the capture cross-section for ^{96,98}Mo(n,γ)^{97,99}Mo is lower than that for^{95,97}Mo(n,γ)^{96,98}Mo, which is usually included in models of the *s*-process in AGB stars. Furthermore, we deduced that, among several NLD and GSF models, the BSFM (for the NLD) and Brink-Axel (for the GSF) of TALYS v1.96 are the best fits for the $^{95-98}$Mo(n, γ)$^{96-99}$Mo process. For these nuclei, the Hauser-Feshbach theory prediction accurately reproduces the available experimental data with parameter modifications.

2. We computed the β^-/positron capture rates based on the *pn*-QRPA framework for different densities and temperatures. The *pn*-QRPA theory effectively calculates the stellar weak interaction rates for $^{96-98}$Mo. Our analysis included a broad model space of 7 $\hbar\omega$. We computed the stellar weak interaction rates within a wide range of temperatures and densities. We noted that at higher densities, the beta decay rates increase with temperature.

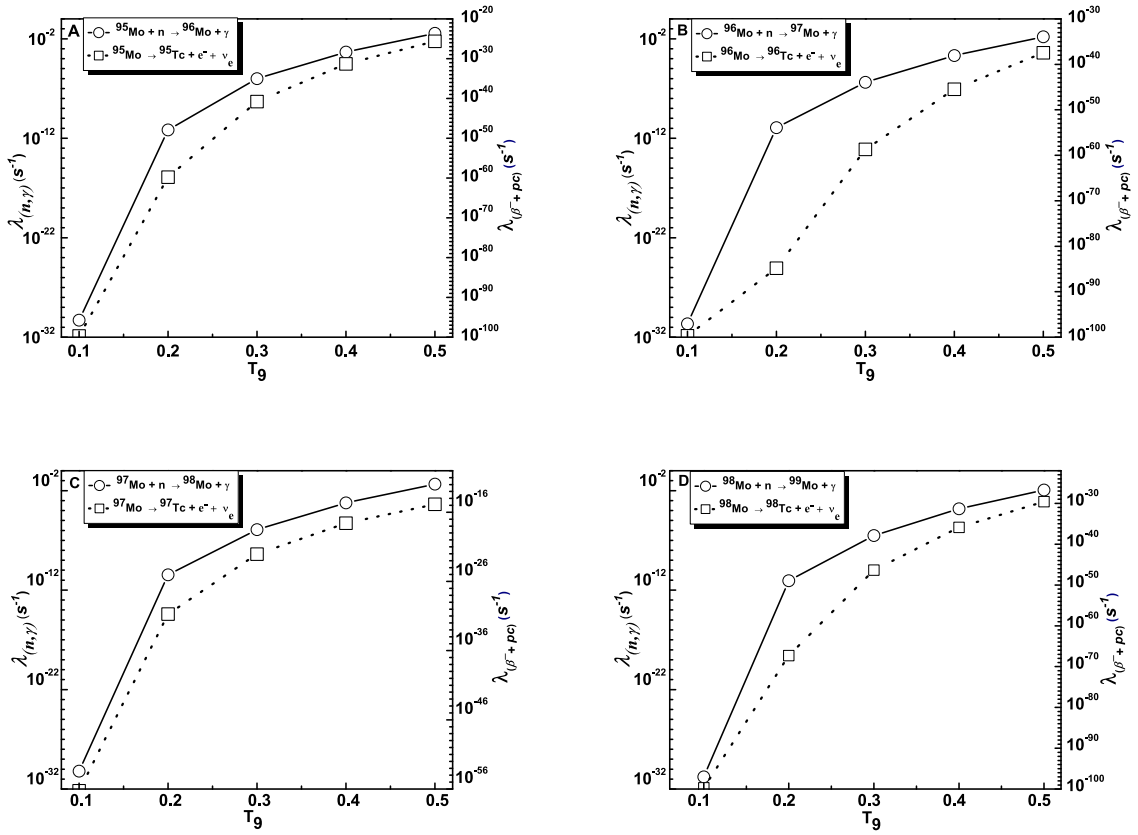

Fig. 7. Neutron capture rates ($\lambda_{(n,\gamma)}$) and stellar beta decay rates ($\lambda_{(\beta^-+pc)}$) of $^{95-98}$Mo at $\rho = 10^4$ g cm^{-3}, $X_4 = 0.2$, and $\sigma_{22} = 0.4$ mb. (A) Computed $\lambda_{(n,\gamma)}$ and $\lambda_{(\beta^-+pc)}$ for ^{95}Mo. (B) Computed $\lambda_{(n,\gamma)}$ and $\lambda_{(\beta^-+pc)}$ for ^{96}Mo. (C) Computed $\lambda_{(n,\gamma)}$ and $\lambda_{(\beta^-+pc)}$ for ^{97}Mo. (D) Computed $\lambda_{(n,\gamma)}$ and $\lambda_{(\beta^-+pc)}$ for ^{98}Mo.

3. We compared $\lambda_{(n,\gamma)}$ and $\lambda_{(\beta^-+pc)}$ under appropriate stellar conditions in the last phase of our investigations. We observed that stellar beta decay rates are lower than neutron capture rates at low and even high temperatures. For example, at T_9 = 0.5, $\lambda_{(n,\gamma)}/\lambda_{(\beta^-+pc)}$ = 1.50×10^{24}, 4.27×10^{35}, 3.22×10^{13}, and 4.48×10^{27} for ^{95}Mo, ^{96}Mo, ^{97}Mo, and ^{98}Mo, respectively. Based on the present investigation, we identified that $\lambda_{(n,\gamma)}$ is higher than λ_{β}.

References

[1] H. A. Bethe, Phys. Rev. **55**, 434 (1939)
[2] E. M. Burbidge *et al*., Rev. Mod. Phys. **29**, 547 (1957)
[3] A. G. W. Cameron, PASP **69**, 201 (1957)
[4] G. M. Fuller *et al*., Astrophys. J **252**, 715 (1982)
[5] W. Baade and F. Zwicky, Proc. Natl. Acad. Sci **20**, 254 (1934)
[6] F. Kappeler *et al*., Astrophys. J **354**, 630 (1990)
[7] S. Dutta *et al*., Phys. Rev. C **94**, 024604 (2016)
[8] H. Pomerance, Phys. Rev **88**(2), 412 (1952)
[9] S. V. Kapchigashev and Y. P. Popov, Soviet Atomic Energy **15**(2), 808 (1964)
[10] C. D. Stupegia *et al*., J. Nucl. Energy **22**(5), 267 (1968)
[11] A. D. Musgrove *et al*., Nucl. Phys. A **270**(1), 108 (1976)
[12] I. Duhamel *et al*., In EPJ Web of Conferences **247**, 09007 (2021)
[13] R. Mucciola *et al*., In EPJ Web of Conferences **284**, 01031 (2023)
[14] C. Massimi, *Measurement of $^{94, 95, 96}$ Mo(n,γ) relevant to Astrophysics and Nuclear Technology*, CERN-INTC-2020-052, INTC-P-569 (2020)
[15] N. V. Do *et al*., Nucl. Instrum. Methods Phys. Res. B **267**, 462 (2009)
[16] M. S. Uddin *et al*., Radiochim. Acta **103**(2), 85 (2015)
[17] S. Bisterzo *et al*., MNRAS **449**, 506 (2015)
[18] H. V. Klapdor-Kleingrothaus, J. Metzinger, and T. Oda, At. Data Nucl. Data Tables **31**, 81 (1984)
[19] J. Krumlinde and P. Möller, Nucl. Phys. A **417**, 419 (1984)
[20] A. Staudt, *et al*., At. Data Nucl. Data Tables **44**, 79 (1990)
[21] M. Hirsch, A. Staudt, and H. V. Klapdor-Kleingrothaus, At. Data Nucl. Data Tables **51**, 243 (1992)
[22] P. Möller and J. Randrup, Nucl. Phys. A **514**, 1 (1990)
[23] P. Möller, J. R. Nix, and K. L. Kratz, At. Data Nucl. Data Tables **66**, 131 (1997)
[24] A. Hektor, E. Kolbe, K. Langanke *et al*., Phys. Rev. C **61**, 055803 (2000)
[25] D. D. Ni and Z. Z. Ren, J. Phys. G **39**, 125105 (2012)
[26] A. J. Koning, S. Hilaire, and S. Goriely, *TALYS–1.96 A Nuclear Reaction Program, User Manual, Nuclear Research and Consultancy Group (NRG)*, Netherlands (2021) http://www.talys.eu.
[27] W. Hauser and H. Feshbach, Phys. Rev **87**, 366 (1952)
[28] S. Goriely, S. Hilaire, and A. J. Koning, A & A **487**, 767 (2008)
[29] D. Rochman, S. Goriely, A. J. Koning *et al*., Phys Lett. B **764**, 109 (2017)
[30] A. J. Koning and J. P. Delaroche, Nucl. Phys. A **713**, 231 (2003)
[31] A. Kabir and J.-U. Nabi, Nucl. Phys. A **1007**, 122118 (2021)
[32] A. Kabir *et al*., Commun. Theor. Phys **74**, 025301 (2022)
[33] B. F. Irgaziev *et al*., Chin. Phys. C **48**(4), 045103 (2024)
[34] A. Kabir *et al*., Braz. J. Phys **54**, 80 (2024)
[35] A. Kabir *et al*., J. Phys. G: Nucl. Part. Phys **49**, 075101 (2022)
[36] A. J. Koning and S. Hilaire, S. Goriely Nucl. Phys. A **810**, 13 (2008)
[37] S. Goriely *et al*., Phys. Rev. C **98**, 014327 (2018)
[38] J. Engel *et al*., Phys. Rev. C **60**, 014302 (1999)
[39] M. Hirsch *et al*., At. Data Nucl. Data Tables **53**, 165 (1993)
[40] H. Homma *et al*., Phys. Rev. C **54**, 2972 (1996)
[41] P. Möller *et al*., Atom. Data Nucl. Data Tables **1090**, 1 (2016)
[42] I. Ragnarsson and R. K. Sheline, Phys. Ser. **29**, 385 (1984)
[43] K. Muto *et al*., Z. Phys. A **333**, 125 (1989)
[44] G. Audi *et al*., Chin. Phys. C **41**, 030001 (2017)
[45] K. Muto *et al*., Z. Phys. A **341**, 407 (1992)
[46] J. U. Nabi and H. V. Klapdor-Kleingrothaus, At. Data Nucl. Data Tables **71**, 149 (1999)
[47] J. U. Nabi and H. V. Klapdor-Kleingrothaus, At. Data Nucl. Data Tables **88**, 237 (2004)
[48] J. C. Hardy and I. S. Towner, Phys. Rev. C **79**, 055502 (2009)
[49] G. J. Mathews *et al*., Astrophys. J **302**, 410 (1986)
[50] R. R. Winters and R. L. Macklin, Astrophys. J **313**, 808 (1987)